

# A Coupled Thermal/Material Flow Model of Friction Stir Welding Applied to Sc-Modified Aluminum Alloys

CARTER HAMILTON, MATEUSZ KOPYŚCIAŃSKI, OLEG SENKOV,  
and STANISLAW DYMEK

A coupled thermal/material flow model of friction stir welding was developed and applied to the joining of Sc-modified aluminum alloy (7042-T6) extrusions. The model reveals that surface material is pulled from the retreating side into the weld zone where it is interleaved with *in situ* material. Due to frictional contact with the shoulder, the surface material is hotter than the *in situ* material, so that the final weld microstructure is composed of bands of material with different temperature histories. For this alloy and the associated FSW heating rates, secondary phase dissolution/precipitation temperatures are in proximity to the welding temperatures. Therefore, depending on the surface and *in situ* material temperatures in relation to these transformation temperatures, disparate precipitate distributions can develop in the bands of material comprising the weld nugget. Based on the numerical simulation and on thermal analysis data from differential scanning calorimetry, a mechanism for the formation of onion rings within the weld zone is presented.

DOI: 10.1007/s11661-012-1512-y

© The Author(s) 2012. This article is published with open access at Springerlink.com

## I. INTRODUCTION

OVER the last 20 years, numerous investigations have sought to characterize the principles of friction stir welding (FSW) and to model the material flow behavior, the temperature distribution, and the microstructural evolution within the weld. The review papers of Nandan *et al.*<sup>[1]</sup> and Threadgill *et al.*<sup>[2]</sup> provide an excellent account of past and current FSW research. Early numerical simulations, such as those of Colegrove and Shercliff<sup>[3]</sup> or Khandkar *et al.*,<sup>[4]</sup> focused on the temperature distribution during welding and studied its potential influence on the weld microstructure and precipitation kinetics. More recently, researchers have been able to model both the material flow behavior and temperature characteristics during FSW despite the complex material flow associated with the process. Robson and Campbell<sup>[5]</sup> developed a grain growth and recrystallization model of FSW that successfully predicted the weld nugget size during the joining of 2524 aluminum alloy plates. Colegrove *et al.*<sup>[6]</sup> created a numerical model that combined material hot deformation and thermal properties to predict temperature, flow stress, and strain rate in age hardenable aluminum

alloys 2024, 7449, and 6013. The current investigation presents a coupled thermal/flow model of friction stir welding applied to Sc-modified Al-Zn-Mg-Cu extrusions (Al alloy 7042-T6).

Additions of scandium (Sc) and zirconium (Zr) to 7000 series alloys stabilize the microstructure at temperatures greater than 423 K (150 °C) through the formation of fine, secondary strengthening phases such as Al<sub>3</sub>(Sc,Zr).<sup>[7,8]</sup> The nanometer-sized Al<sub>3</sub>(Sc,Zr) particles also stabilize the microstructure formed during hot working operations and inhibit recrystallization during heat treatment, thus potentially enhancing the residual properties after joining operations such as FSW.<sup>[9]</sup> These additions also affect the kinetics of precipitation and growth of the primary strengthening precipitates (GP zones,  $\eta'$ ), thus modifying heat treatment conditions for enhancing the mechanical properties of these alloys.<sup>[10]</sup> The numerical simulation proposed here gives insight into the material flow and temperature distribution of the weld zone during the joining of 7042-T6 extrusions. Combined with thermal analysis data from differential scanning calorimetry (DSC), the precipitation behavior within the weld is discussed in terms of the volume fraction of the metastable (GP zones and  $\eta'$ ) and equilibrium [ $\eta$  (MgZn<sub>2</sub>) and/or T (Al<sub>2</sub>Mg<sub>3</sub>Zn<sub>3</sub>)] strengthening particles found in the 7042 aluminum alloy.<sup>[11]</sup> It is assumed that FSW does not change the size and volume fraction of the Al<sub>3</sub>(Sc,Zr) precipitates due to their high thermal stability.<sup>[12]</sup>

DSC is a powerful technique for the investigation of precipitation and dissolution processes in Al alloys.<sup>[10,13]</sup> By detecting the heat variations due to the phase transformations, the technique is able to identify the temperature ranges in which they occur. For example, Dixit *et al.*<sup>[14,15]</sup> utilized DSC to study the nucleation of precipitates within the nugget of friction stir welded

---

CARTER HAMILTON, Associate Professor, is with the Department of Mechanical and Manufacturing Engineering, Miami University, Oxford, OH. Contact e-mail: hamiltbc@muohio.edu  
MATEUSZ KOPYŚCIAŃSKI, Ph.D. Candidate, and STANISLAW DYMEK, Professor and Chair, are with the Faculty of Metals Engineering and Industrial Computer Science, AGH University of Science and Technology, Kraków, Poland. OLEG SENKOV, Senior Scientist, is with UES, Inc., 4401 Dayton-Xenia Rd, Dayton, OH, 45432-1894

Manuscript submitted April 10, 2012.

Article published online November 9, 2012

aluminum 2024 and to correlate the weld microstructure to mechanical properties. In the present work, results of the DSC thermal analysis of the FSW regions of the 7042-T6 Al alloy, together with a developed coupled thermal/material flow model of FSW, were used to propose a mechanism of onion ring formation within the weld zone. The model reveals that surface material is pulled from the retreating side into the weld zone where it is interleaved with *in situ* material.

## II. EXPERIMENTAL PROCEDURE

### A. Alloy Chemistry and Heat Treatment

The chemical composition of the 7042-T6 Al alloy used in this work is given in Table I. This alloy utilizes the synergistic combination of scandium and zirconium to stabilize the microstructure and enhance mechanical properties. For this investigation, a 76-mm diameter 7042 billet was produced by direct chill casting and then hot extruded into a bar with a rectangular cross section of 50.4 mm × 6.35 mm, thus providing the extrusion ratio of 14:1. Following extrusion, the bar was heat treated to a T6 temper through the following schedule: (1) solution heat treat at 733 K (460 °C) for 1 hour followed by an additional hour at 753 K (480 °C), (2) rapid quench in water to room temperature, and (3) age at 393 K (120 °C) for 19 hours.

### B. Friction Stir Welding

After heat treatment, the bar was cut into twelve, 305-mm-long pieces and sent to the Edison Welding Institute (EWI, Columbus, OH) to produce six longitudinal friction stir welds. The diameter of the FSW tool shoulder was 17.8 mm, the pin diameter tapered linearly from 10.3 mm at the tool shoulder to 7.7 mm at the tip, and the pin depth was 6.1 mm. With a constant weld velocity of 2.1 mm s<sup>-1</sup> and a constant applied force of 22 kN, unique welds were produced at the following pin rotation speeds (PRS): 175, 225, 250, 300, 350, and 400 rev min<sup>-1</sup>. The temperature profile across the weld surface was experimentally recorded for each condition using a Mikron M7815 Infrared Thermal Imaging Camera during welding. These data were used to verify the temperature

predictions of the coupled thermal/flow simulation developed during this investigation. The uncertainty in these measurements was ±2 pct (or approximately ±9 K). The thermal emissivity for the infrared data was calibrated by imaging an extrusion length heated to 733 K (460 °C) and adjusting the emissivity value until the recorded temperature of the camera matched the reference temperature. The appropriate thermal emissivity value was determined to be 0.285.

### C. Post-Weld Investigation

Subsequent to joining, the welded panels were stored at room temperature and allowed to naturally age for at least 30 days prior to testing and investigation. Small samples (approximately 20 to 50 mg) were extracted from the T6-tempered baseline material and from the weld center of each welded sample for thermal analysis. The samples were sealed in Al pans and analyzed in a Perkin Elmer Jade differential scanning calorimeter, using an argon atmosphere. Depending on the data desired, samples were heated from room temperature to 673 K (400 °C) at a constant heating rate that ranged from 10 to 100 K min<sup>-1</sup>. A polarized optical microscope was used to study the microstructure of the welds. To enhance the appearance of precipitate distributions and grains, the studied surfaces of the weld samples were polished and anodized in an electrolytic solution of 1.8 pct fluoroboric acid in water at room temperature and an electric current of 0.15 A. The anodizing time was 2.5 to 3 minutes.

## III. COUPLED MODEL FOR FLOW AND TEMPERATURE BEHAVIOR

### A. Materials Properties and Boundary Conditions for Flow

A coupled thermal/flow model was developed for friction stir welding utilizing the Comsol multi-physics software. Figure 1 displays the model utilized to simulate the thermal/flow characteristics of the FSW process (the meshed model is shown as an inset). Tetrahedral elements were primarily utilized for meshing, giving 31,845 tetrahedral, 6928 triangular, 1118 edge, and 91 vertex elements. As indicated in the figure, the model defines a flow-capable region between the advancing and retreating sides in which the temperature and action of the tool plasticizes the aluminum workpiece, and material flow occurs. The width of the flow-capable region is set 1 mm wider than the tool shoulder to permit limited bypass flow around the shoulder at the workpiece surface. The inlet velocity into the flow region is simply the weld velocity,  $u_{\text{weld}}$ , defined in the positive  $x$ -direction (actual tool displacement occurs in the negative  $x$ -direction, but the inlet velocity effectively captures tool articulation in the simulation). The boundary condition for the velocity field between the flow region and the advancing side, the retreating side, and the backing spar is no slip, and these interfaces have mirrored meshes to insure continuity in the thermal

Table I. Chemical Composition of 7042

Element	Weight Percent	
	7042, This Work	7042, Nominal
Zn	7.11	6.5–7.9
Mg	2.14	2.0–2.8
Cu	1.56	1.3–1.9
Mn	0.25	0.2–0.4
Zr	0.17	0.11–0.20
Sc	0.38	0.18–0.50
Cr	< 0.05	≤0.05
Ti	—	—
Other, Total	0.35	≤0.55
Al	balance	

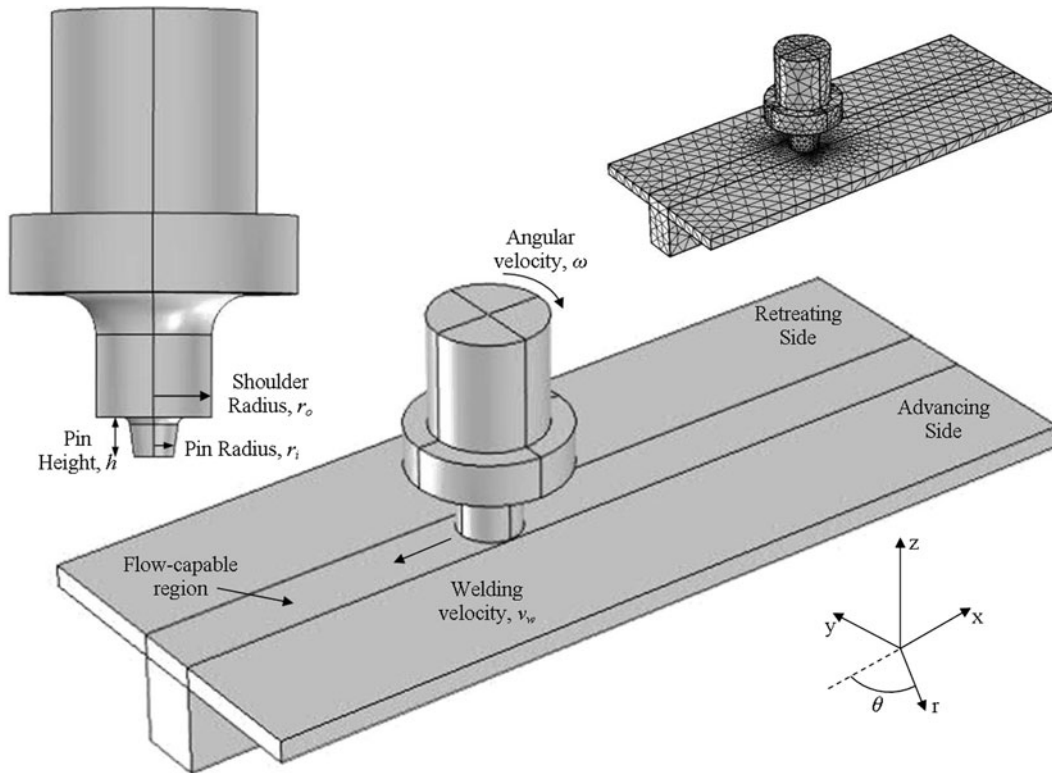


Fig. 1—Computational solid model of the friction stir welding process.

distribution across the boundaries (the thermal boundary conditions are discussed in greater detail in the subsequent section). The velocity boundary condition for the surface of the flow region is

$$u = u_{\text{weld}}, \quad v = 0, \quad w = 0 \quad [1]$$

where  $u$ ,  $v$ , and  $w$  are the conventional representations of the velocity magnitudes in the  $x$ -,  $y$ -, and  $z$ -directions, respectively.

As also shown in Figure 1, there are effectively four boundaries between the tool and the flow-capable region. These are (1) the tool shoulder, (2) the fillet radius between the shoulder and pin, (3) the pin side, and (4) the pin bottom. The velocity field boundary conditions for the tool shoulder, the fillet radius, and the pin bottom are the same and are given in the following equation:

$$u = \omega y, \quad v = -\omega x, \quad w = 0 \quad [2]$$

where  $\omega$  is the angular velocity of the tool. Though not actually rendered in the solid model shown in Figure 1, the pin is threaded with a pitch value,  $p$ , of 1.27 mm. Therefore, the boundary condition for the pin side can account for the vertical displacement of material per tool revolution due to the threads and is given by

$$u = \omega y, \quad v = -\omega x, \quad w = -p \left( \frac{\omega}{2\pi} \right) \quad [3]$$

To solve for the velocity field within the flow region, the viscosity of the region,  $\mu$ , must be known. The

viscosity is determined from the flow stress,  $\sigma_e$ , and the effective strain rate,  $\dot{\epsilon}$  through the following relationship:<sup>[16]</sup>

$$\mu = \frac{\sigma_e}{3\dot{\epsilon}} \quad [4]$$

The maximum strain rates within the flow region occur adjacent to the weld tool, *i.e.*, under the tool shoulder and along the pin, where the velocity gradients are the greatest. The strain rates decrease rapidly away from the tool since the material flow velocities also decrease quickly away from the tool. In their work on aluminum, Frigaard *et al.*<sup>[17]</sup> estimated the maximum effective strain rate under the tool shoulder to be  $20 \text{ s}^{-1}$ , while Nandan *et al.*<sup>[18]</sup> calculated the maximum strain rate as  $100 \text{ s}^{-1}$  near the tool shoulder and as  $30 \text{ s}^{-1}$  approximately 4 mm below the shoulder. More recently, Arora *et al.*<sup>[19]</sup> computed the maximum strain rate in aluminum 2524 as  $9 \text{ s}^{-1}$  for their FSW parameters and tools. Colegrove *et al.*<sup>[6]</sup> used constant strain rate values ranging from  $0.001$  to  $1000 \text{ s}^{-1}$  in their thermal/flow simulations of aluminum alloys.

In this study, the calculation of viscosity and flow stress is simplified by assuming a constant, maximum value for the effective strain rate calculated at the tool shoulder that is then applied to the entire flow-capable region. This approach overestimates the strain rates away from the tool shoulder and pin, but still accurately captures the material flow behavior in the vicinity of the tool. As noted by Colgrove,<sup>[6]</sup> the tool surface dominates both heat generation and process kinematics; therefore,

using a constant, maximum strain rate value derived from the tool shoulder provides a good approximation of the phenomena occurring in the entire weld region. To determine this value, assume that the velocity components  $u$  and  $v$  decrease linearly from the tool shoulder to the bottom of the workpiece as suggested by Heurtier *et al.*<sup>[20]</sup> and that the velocity component  $w$  remains constant. The velocity field in the area under the tool shoulder and adjacent to the pin then approximately becomes (with  $z = 0$  located at the workpiece bottom for convenience)

$$u = \omega y \left( \frac{z}{h} \right) - u_{\text{weld}}, v = -\omega x \left( \frac{z}{h} \right), w = -p \left( \frac{\omega}{2\pi} \right) \quad [5]$$

where  $h$  is the workpiece thickness. Nandan *et al.*<sup>[18]</sup> provide the expanded form of the effective strain rate as a function of the velocity gradients, and applying this to Eq. [5] yields the following expression for the effective strain rate:

$$\begin{aligned} \dot{\epsilon} &= \sqrt{\left( \frac{2}{3} \left( \frac{\partial u}{\partial z} + \frac{\partial w}{\partial x} \right)^2 + \frac{1}{2} \left( \frac{\partial v}{\partial z} + \frac{\partial w}{\partial y} \right)^2 \right)} \\ &= \sqrt{\frac{1}{3} \left( \frac{w^2 y^2}{h^2} + \frac{w^2 x^2}{h^2} \right)} \end{aligned} \quad [6]$$

Evaluating  $x$  and  $y$  in Eq. [6] at the tool shoulder radius,  $r_{\text{shoulder}}$ , yields the following expression for the maximum effective strain rate:

$$\dot{\epsilon} = \frac{r_{\text{shoulder}} \sqrt{6}}{3h} \omega \quad [7]$$

For the process parameters utilized in this investigation, the maximum effective strain rate varies from  $20.9 \text{ s}^{-1}$  at  $175 \text{ rev min}^{-1}$  to  $47.9 \text{ s}^{-1}$  at  $400 \text{ rev min}^{-1}$ . These numbers certainly fall within the range of effective strain rate values calculated and utilized by other researchers.

Sheppard and Wright<sup>[21]</sup> proposed a formulation for the flow stress in Eq. [4] as

$$\sigma_e = \frac{1}{\alpha} \sinh^{-1} \left[ \left( \frac{Z}{A} \right)^{\frac{1}{n}} \right] \quad [8]$$

where  $A$ ,  $\alpha$ , and  $n$  are material constants and  $Z$  is the Zener–Hollomon parameter that captures the temperature influence on the effective strain rate:

$$Z = \dot{\epsilon} \exp \left( \frac{Q}{RT} \right) \quad [9]$$

**Table II. Material Constants for the Sheppard and Wright Flow Stress Equation and the Zener–Hollomon Parameter<sup>[6]</sup>**

Material Constant	Value	Units
$Q$	134158.4	$\text{J mol}^{-1}$
$A$	$1.26 \times 10^8$	$\text{s}^{-1}$
$\alpha$	0.03055	$\text{MPa}^{-1}$
$n$	3.24644	n/a

where  $Q$  is the activation energy,  $R$  is the universal gas constant, and  $T$  is the absolute temperature. The values for  $Q$ ,  $A$ ,  $\alpha$ , and  $n$  presented in Table II were taken from Colegrove *et al.*<sup>[6]</sup> for aluminum 7449. During the simulation, the Zener–Hollomon parameter is recalculated for each iteration based upon the predicted welding temperature. As such, the model captures the temperature dependence of the effective strain rate, the flow stress, and the viscosity during friction stir welding.

## B. Materials Properties and Boundary Conditions for Temperature

Within the flow-capable region of the modeled aluminum workpiece, the heat transfer and material flow behavior are coupled. The thermal properties, *i.e.*, the thermal conductivity,  $k$ , and the specific heat capacity,  $c_p$ , within the flow region are identical to those within the retreating and advancing sides (indicated in Figure 1) of the aluminum workpiece. These thermal properties, as well as those of the tool and backing spar, and their temperature dependence are shown in Figure 2.<sup>[22]</sup> The tool/workpiece slip behavior and heat flux calculations for the tool shoulder and pin bottom, the primary sources for heat generation during FSW, are presented in Reference 22. The heat flux equations, however, have been modified to represent heat flux values averaged over the tool shoulder,  $q_{\text{shoulder}}$ , and pin

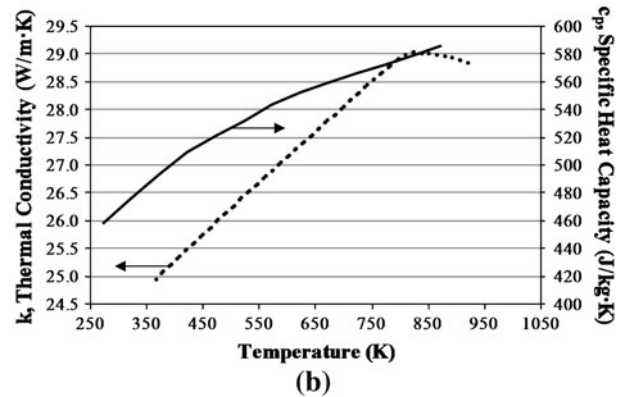
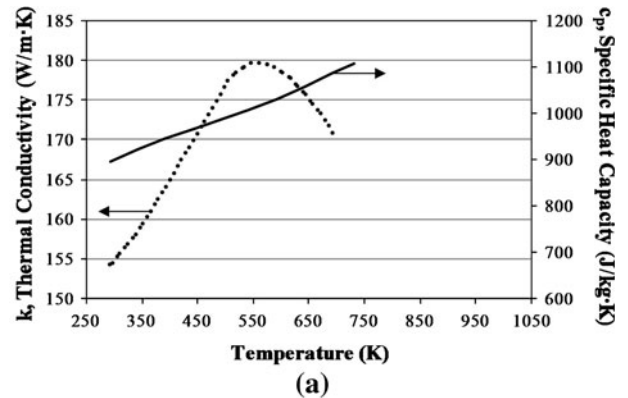


Fig. 2—Temperature-dependent behavior of thermal conductivity and specific heat capacity for (a) workpiece material and (b) tool and backing spar material.

bottom,  $q_{\text{pinbottom}}$ , areas (area-averaged) rather than line-averaged on the radius as presented in this paper. The modified equations are

$$q_{\text{shoulder}} = \frac{2}{3} \delta_E \mu P_N \omega r_{\text{pin}} \quad [10]$$

$$q_{\text{pinbottom}} = \frac{2}{3} \frac{\delta_E \mu P_N \omega (r_{\text{shoulder}}^3 - r_{\text{pin}}^3)}{r_{\text{shoulder}}^2 - r_{\text{pin}}^2} \quad [11]$$

where  $\omega$  is the angular velocity of the tool,  $r_{\text{pin}}$  is the radius of the tool pin,  $r_{\text{shoulder}}$  is the radius of the tool shoulder,  $\mu$  is the coefficient of friction between tool and workpiece,  $P_N$  is the applied pressure on the workpiece during welding, and  $\delta_E$  is the tool slip factor ( $\mu$ ,  $P_N$ , and  $\delta_E$  are defined in greater detail in Reference 22).

A thermal insulation constraint is applied at each interface of the flow-capable region with the non-flow areas of the model, *i.e.*, with the retreating side, with the advancing side and with the backing spar. These constraints assure temperature continuity across the flow-capable boundaries into the other areas of the model. Thermal insulation constraints are also applied to the tool shoulder/workpiece and pin bottom/workpiece interfaces to assure heat continuity across these boundaries as well. For the boundaries exposed to ambient conditions, *i.e.*, the workpiece top, workpiece side, and tool side, the convective heat transfer coefficient is set to  $15 \text{ W/m}^2 \text{ K}$  to approximate free convection on these surfaces. As suggested in References 22 and 23, convection coefficients of 200 and  $250 \text{ W/m}^2 \text{ K}$  are applied to the tool top and spar bottom, respectively. For the underside of the workpiece and the sides of the backing spar, a convective coefficient of  $100 \text{ W/m}^2 \text{ K}$  is used to represent the dissipation of heat into the backing plate. Heat dissipation due to radiation is ignored in this model.

### C. Model Verification

Figure 3 plots the experimental temperature profiles for the advancing side captured by the thermal imaging camera for the  $400 \text{ rev min}^{-1}$  (Figure 3(a)) and  $250 \text{ rev min}^{-1}$  (Figure 3(b)) conditions with those profiles predicted by the coupled thermal/flow model. The profiles selected within the model begin at the weld line 5 mm ahead of the tool center (in the negative  $x$ -direction according to Figure 1) and extend along the surface of the advancing side to a distance of 37.5 mm. Near the tool and the flow-capable region, the model shows very good agreement with the magnitude and shape of the experimental data for both welding conditions. For the  $400 \text{ rev min}^{-1}$  condition, *i.e.*, higher weld energies, in particular, the agreement between the model and the experimental surface temperature profile extends even to distances more than 35 mm away from the weld line. For the  $250 \text{ rev min}^{-1}$  condition, *i.e.*, lower weld energies, the profile is in excellent agreement with the experimental data up to 10 mm from the weld line, but the model then overpredicts the surface temperatures away from the center line and tool. The dissipative

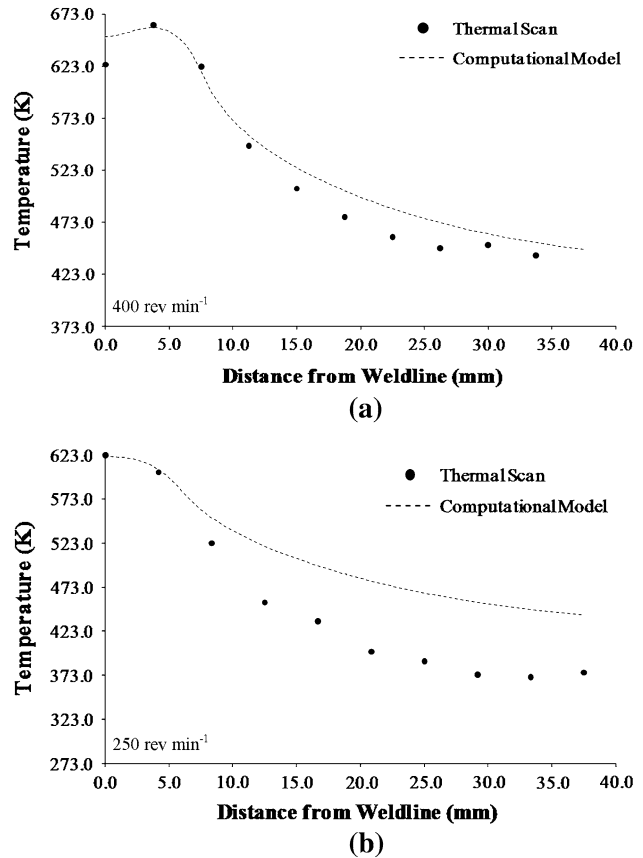


Fig. 3—Experimental temperature and predicted temperature profiles: (a)  $400 \text{ rev min}^{-1}$  and (b)  $250 \text{ rev min}^{-1}$ .

cooling within the workpieces away from the weld may be greater than simulated by the computational model. However, due to the agreement between the model and experimental data within the flow-capable and tool regions for both high and low weld energies, the coupled thermal/flow model is able to analyze the thermal and material flow behavior of the 7042 Al alloy during friction stir welding.

## IV. RESULTS AND DISCUSSION

### A. Material Flow and Temperature Distribution

Figure 4 from the simulation shows the three-dimensional flow behavior of surface material “tracers” during the friction stir welding process (representatively shown for the  $400 \text{ rev min}^{-1}$  condition). The color shading indicates the tracer temperature during the material flow. Ahead of the advancing tool, surface material is swept toward the retreating side of the weld. From here, the tracers follow three primary paths: (1) tracers are carried on the surface along the tool shoulder toward the advancing side and deposited behind the tool, (2) tracers are trapped by the rotating tool and remain on the surface under the tool shoulder, and (3) tracers are pulled by the pin/shoulder from the retreating side of the surface down into the weld zone.

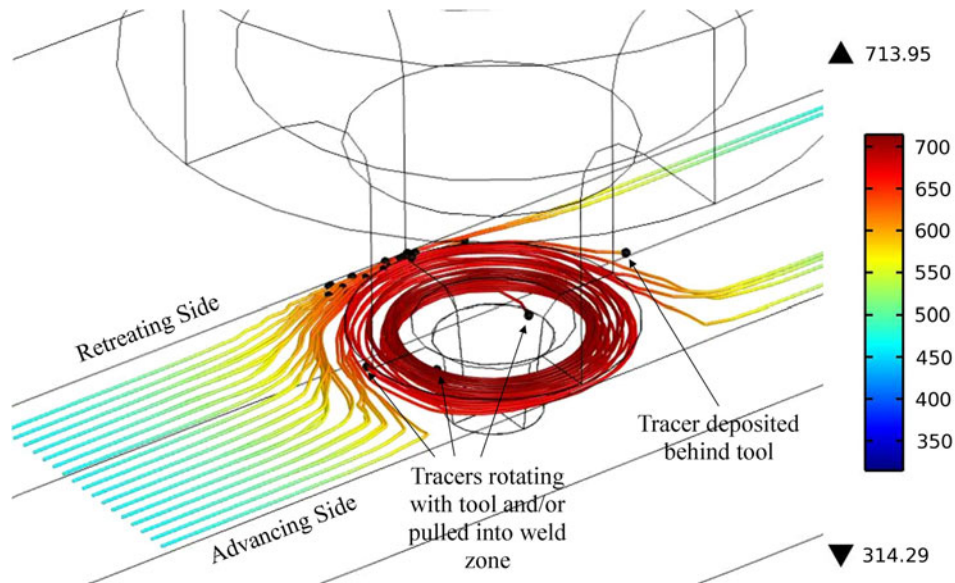


Fig. 4—Flow and temperature (K) behavior of surface material tracers during FSW (400 rev min<sup>-1</sup> shown).

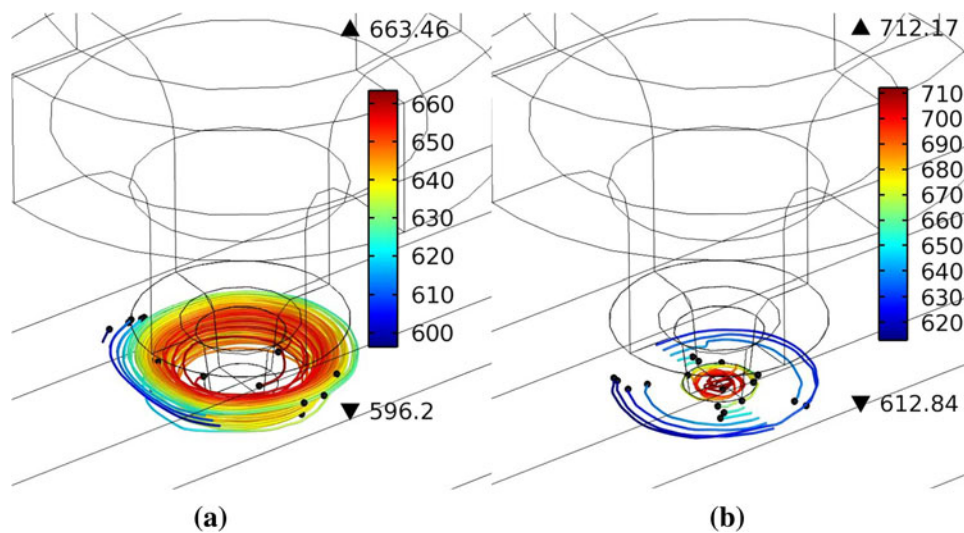


Fig. 5—Flow and temperature (K) behavior of (a) mid-plane tracers and (b) bottom plane tracers (400 rev min<sup>-1</sup> shown).

These numerical results of material flow are consistent with the experimental observations of other researchers. Hamilton *et al.*<sup>[24]</sup> studied the friction stir welding of 6101-T6 extrusions plated with tin (0.05-mm thick). After welding, the unique presence of tin within the weld nugget and the lack of tin within the TMAZ led them to conclude that the weld nugget forms as surface material is extruded from the retreating side into a region of plasticized material around the FSW pin and under the tool shoulder. Colligan,<sup>[25]</sup> in his study of material flow during the FSW of 6061-T6, used steel shot tracers and concluded that surface material extrudes from the retreating side of the pin and deposits in the wake of the tool. Guerra *et al.*,<sup>[26]</sup> in their study of FSW of 6061, utilized a faying surface tracer and similarly hypothesized that material from the front of the retreating side of the pin extrudes between the deformed surface

material rotating with the tool and the parent material into the area behind the pin.

Figure 5a shows the simulated three-dimensional material flow behavior of mid-plane (relative to the workpiece) material tracers during the process (also representatively shown for the 400 rev min<sup>-1</sup> condition). Here, “*in situ*” tracers are primarily trapped by the rotating pin and either remain at the mid-plane level rotating with the pin or are pulled toward the bottom of the workpiece. Similarly, Figure 5b shows the simulated flow behavior of bottom plane material tracers and reveals that these tracers also rotate with the pin or migrate under the pin bottom and rotate with the tool at this level. These numerical results of material flow show good agreement with Reynolds’ experimental model of FSW as an extrusion process where the tool shoulder, pin, backing plate, and base metal effectively form an

“extrusion chamber”.<sup>[27]</sup> However, the tracers utilized in Reynolds’ study of material flow also revealed a downward motion of surface material on the advancing side coupled with the vertical rise of material from the bottom surface of the retreating side within the pin diameter. This type of flow behavior is not captured by the numerical simulation presented here.

Examination of the temperature distribution from the numerical simulation demonstrates that the advancing side is hotter than the retreating side of the weld, albeit by a small magnitude. Figure 6 shows the temperature transient for two points located on the weld surface at the same  $x$ - and  $z$ -coordinates relative to the tool center, but one is located on the advancing side and the other on the retreating side of the weld. As shown in the figure, the advancing side temperature is 5 to 10 K hotter than that of the retreating side. As the tool advances during FSW, cooler material in front of the tool is swept to the retreating side, while material that is rotated around and heated by the tool is deposited behind the tool toward the advancing side. This flow of material effectively raises the advancing side temperature above that of the retreating side. In a separate study of friction stir welded 7042-T6, Hamilton *et al.*<sup>[28]</sup> noted that tensile samples extracted from the welded plates fractured toward the advancing side, suggesting that the advancing side was softer than both the weld center and retreating side. Through DSC analysis of samples taken from the weld, they hypothesized that the advancing side temperature reaches an endothermic transformation temperature before the retreating side, *i.e.*, the advancing side is hotter, and becomes depleted in strengthening precipitates.

Perhaps this result is more clearly illustrated by the inset to Figure 6. Here, a two-dimensional coupled thermal/flow model for aluminum flowing around a rotating, heat-generating circular boundary is presented. The streamlines in the inset show that, like in the three-dimensional FSW model for 7042-T6, cooler material ahead of the rotating boundary is swept to the retreating side and material heated by the boundary is deposited on the advancing side. As a result, the temperature distribution is skewed, and higher temperatures develop on the advancing side.

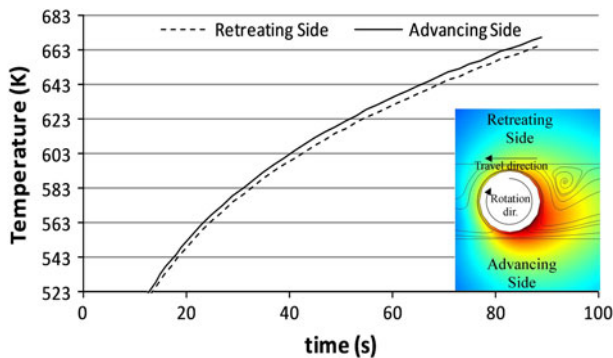


Fig. 6—Temperature comparison of the retreating and advancing sides during FSW (inset: 2D model demonstrating temperature skew toward the advancing side).

## B. Formation of Onion Rings

In their differential thermal analysis through DSC, Hamilton *et al.*<sup>[28]</sup> demonstrated that three phase transformations occur in the 7042-T6 alloy during heating at 10 K/min between room temperature and 673 K (400 °C). These are (i) an endothermic transformation occurring near 438 K (165 °C) and caused by the dissolution of the non-equilibrium GP zones and  $\eta'$  particles, (ii) an exothermic transformation occurring near 489 K (216 °C) and caused by the formation and growth of the equilibrium  $\eta$  and/or  $T$  phases, and (iii) an endothermic transformation occurring above  $\sim$ 523 K (250 °C) due to dissolution of these equilibrium phases.<sup>[10–13]</sup> Hamilton *et al.*<sup>[28]</sup> further noted that since the dissolution and formation of secondary phases are thermally activated processes, the positions of the endothermic and exothermic peaks, corresponding to the maximum rates of the reactions, will shift to higher temperatures with increasing heating rates. During friction stir welding, therefore, the high heating rates can shift these phase reaction temperatures to values in the proximity of the welding temperatures, significantly impacting the final microstructure. Based on their work, Table III presents the estimated endothermic and exothermic peak transformation temperatures for each weld condition, *i.e.*, FSW heating rate, at both the weld edge and the weld center. It can be seen that with an increase in the pin rotation speed from 175 to 400 rev min<sup>-1</sup>, the peak temperature of the dissolution of the non-equilibrium GP and  $\eta'$  phases increases from 548 K to 557 K (275 °C to 284 °C) in the weld edge and from 563 K to 571 K (290 °C to 298 °C) in the weld center, while the peak temperature of formation and growth of the  $\eta$  and/or  $T$  phases increases from 602 K to 609 K (329 °C to 336 °C) in the weld edge and from 617 K to 625 K (344 °C to 352 °C) in the weld center. One may therefore conclude that at the same welding condition, the maximum rates of the phase reactions in the weld center occur at slightly higher ( $\sim$ 15 K) temperatures than in the weld edge.

**Table III. Endothermic and Exothermic Peak Transformation Temperatures Estimated (From DSC Data) for Different Weld Conditions at the Weld Edge (Retreating Side) and Weld Center.<sup>[28]</sup>**

Welding Condition (rev min <sup>-1</sup> )	Endothermic Transformation Temperature [K (°C)]	Exothermic Transformation Temperature [K (°C)]
<b>Weld Edge (Retreating Side)</b>		
175	548 (275)	602 (329)
225	550 (277)	603 (330)
250	551 (278)	604 (331)
300	554 (281)	608 (335)
350	556 (283)	609 (336)
400	557 (284)	609 (336)
<b>Weld Center</b>		
175	563 (290)	617 (344)
225	565 (292)	618 (345)
250	566 (293)	619 (346)
300	569 (296)	623 (350)
350	571 (298)	624 (351)
400	571 (298)	625 (352)

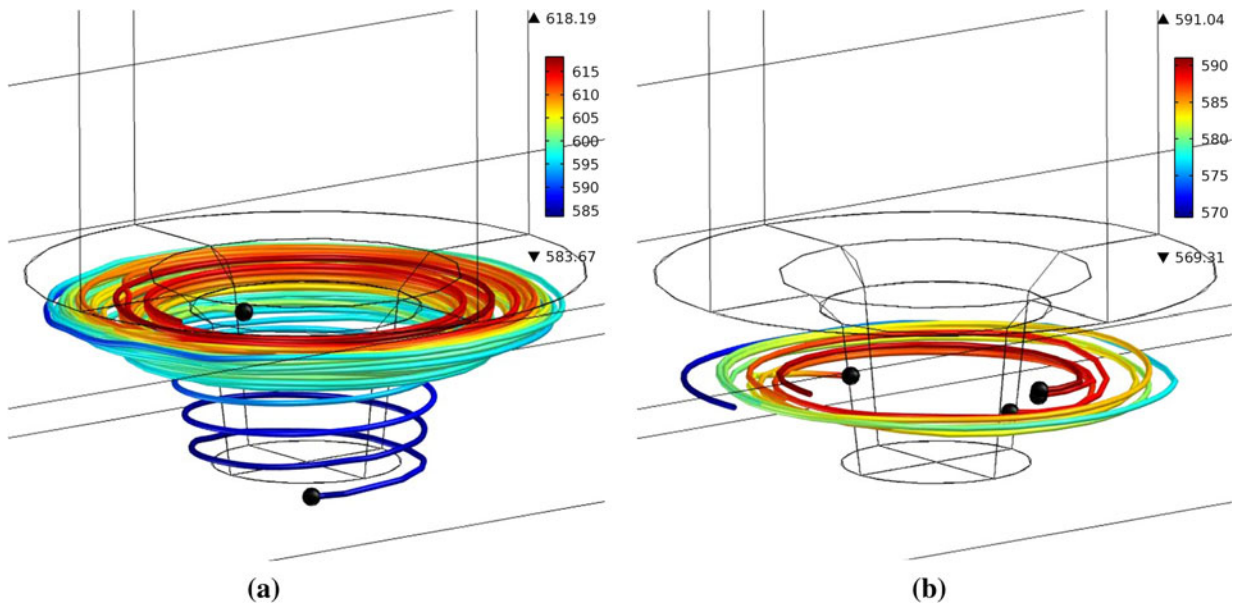


Fig. 7—Flow and temperature (K) behavior of (a) surface material tracers pulled into the weld zone and (b) mid-plane tracers that rotate around the pin (250 rev min<sup>-1</sup> shown).

Figure 7a presents the material flow behavior of surface material tracers during the 250 rev min<sup>-1</sup> condition with color shading indicating the temperature history. As seen in the figure, surface tracers under the shoulder and near the weld edge can reach temperatures of 618 K (345 °C), temperatures just greater than or approximately equal to the weld edge exothermic reaction temperature [604 K (331 °C)] for this weld condition. As such, the material represented by these tracers becomes enriched in the equilibrium  $\eta$  and/or T phase particles before being pulled by the screw action of the pin from the retreating side into the weld zone. These  $\eta$ /T particles are much coarser than non-equilibrium GP zones and  $\eta'$  particles. Upon cooling, the equilibrium phase particles are retained, forming bands of material that appear “particle-rich” under light/scanning electron microscopy within the weld zone.

In contrast, the *in situ*, mid-plane material tracers of the weld zone (Figure 7(b)) only reach temperatures of ~593 K (320 °C) near the pin surface and close to the weld center during the 250 rev min<sup>-1</sup> condition. These temperatures are greater than the weld center endothermic reaction temperature [566 K (293 °C)], but certainly less than the weld center exothermic transformation temperature [619 K (346 °C)]. As such, the *in situ* weld material becomes depleted in the non-equilibrium  $\eta'$  phase (due to dissolution of GP zones and  $\eta'$  particles) and also becomes supersaturated with solute elements upon cooling since the precipitation of the  $\eta$  and/or T phases never takes place. Upon cooling, re-precipitation of fine GP zones occurs within the *in situ* weld material, forming bands of material that appear “particle-poor” under light/scanning electron microscopy within the weld zone (the nanometer-sized GP zones cannot be distinguished under light microscopy or even conventional SEM conditions). The final weld microstructure, therefore, is comprised of coarse-particle-rich bands of

material pulled from the surface’s retreating side and interleaved with coarse-particle-poor bands of the *in situ* weld material, imparting an onion ring appearance. Figure 8 presents SEM images of the 250 rev min<sup>-1</sup> weld and reveals these distinct bands of particle-rich and particle-poor material comprising the weld microstructure and creating the onion ring structure.

The potential for onion ring formation in the 7042-T6 alloy therefore depends on the surface and *in situ* material temperatures relative to the endothermic and exothermic reaction temperatures in these regions for the given weld conditions. If both the surface and *in situ* material temperatures are less or greater than the exothermic temperature, then the appearance of onion rings is minimized. In the first case, no coarse particles will form in both regions, while in the second case, similar coarse particles will form in both regions; thus, low optical contrast between the regions will develop. If, however, one of the surface and *in situ* material temperatures is below and another is above the peak exothermic transformation temperature, then onion ring formation is maximized since each material zone will exhibit unique precipitation characteristics.

The weld conditions leading to the formation of the onion rings are clearly illustrated in Figure 9. In this figure, the temperature differences ( $\Delta T = T_W - T_P$ ) between the surface or *in situ* material temperatures,  $T_W$ , and the respective peak exothermic transformation temperature,  $T_P$ , are plotted versus the tool rotation speed. The surface temperature is taken at a computational point located 0.85 mm below the actual workpiece surface and 7.00 mm from the tool center; the *in situ* temperature is taken at a point 3.18 mm below the workpiece surface and 7.00 mm from the tool center; and peak exothermic transformation temperatures are taken from Table III (weld center peaks are taken for *in situ* material and weld edge peaks are taken for



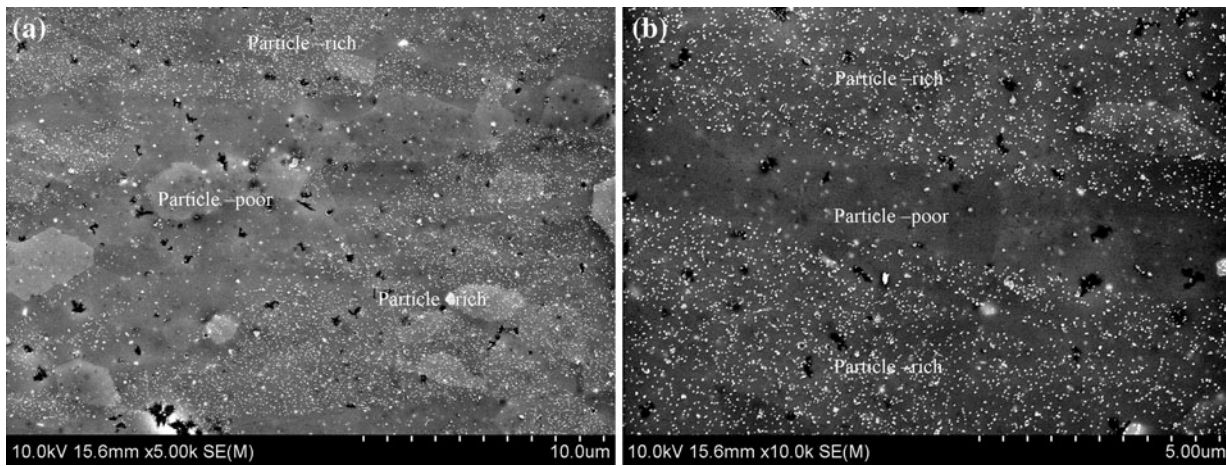


Fig. 8—SEM images of the 250 rev min<sup>-1</sup> weld revealing the particle-rich and particle-poor bands of the onion ring structure: (a) 5000× and (b) 10,000×.

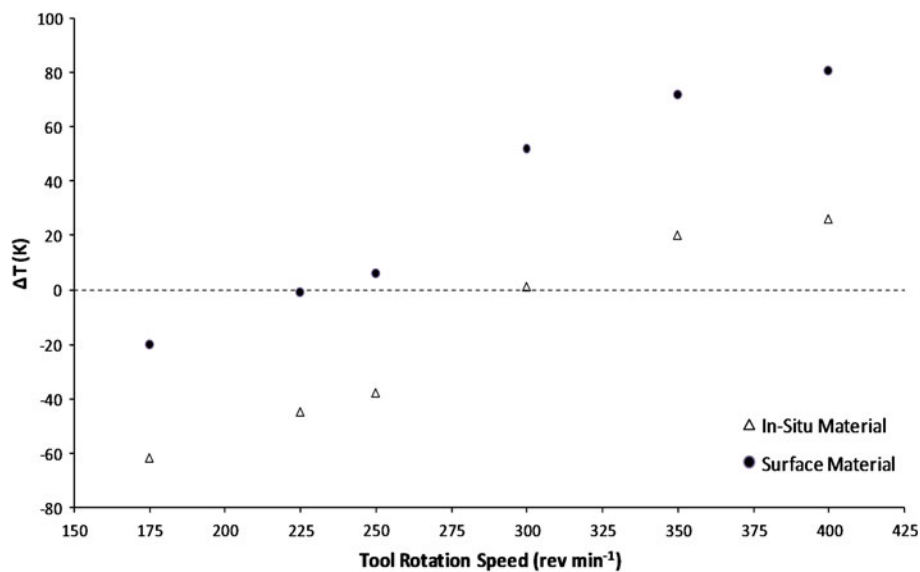


Fig. 9—The surface and *in situ* material temperatures relative to the respective peak exothermic transformation temperatures (Table III) as functions of the tool rotation speed.

surface material). A horizontal line at  $\Delta T = 0$  corresponds to the condition when the material's temperature at a given coordination point and weld condition is equal to the respective peak exothermic transformation temperature.

For welding at 175 rev min<sup>-1</sup>, the *in situ* material's temperature is ~60 K and the surface material's temperature is ~20 K below the respective exothermic reaction temperatures ( $\Delta T$  is negative in both cases, see Figure 9). This suggests that no visible coarse  $\eta/T$  particles would form in either region, and thus onion rings would not develop for this weld condition. Indeed, the metallographic image of the 175 rev min<sup>-1</sup> weld zone presented in Figure 10 reveals a primarily uniform microstructure. However, a faint onion pattern can still be seen, which probably indicates that precipitation of the  $\eta/T$  particles has already started at the surface region.

At 225 rev min<sup>-1</sup>, the *in situ* material temperature is greater than the endothermic reaction temperature, but about 45 K smaller than the peak exothermic temperature. On the other hand, the surface material temperature corresponds to the peak exothermic reaction temperature. The *in situ* material will again be free of the  $\eta/T$  particles. However, the rate of formation of these particles now reaches a maximum value in the surface material before it is pulled from the retreating side down into the nugget. These stable secondary phases are retained in the microstructure upon cooling, thus creating the potential for onion ring formation due to the difference in precipitation behavior between the material zones. Examination of the metallographic image of the 225 rev min<sup>-1</sup> weld (Figure 10) reveals the emergence of a more prominent onion ring pattern.

The onion rings are most pronounced for the 250 and 300 rev min<sup>-1</sup> welds, as illustrated in Figure 10. As

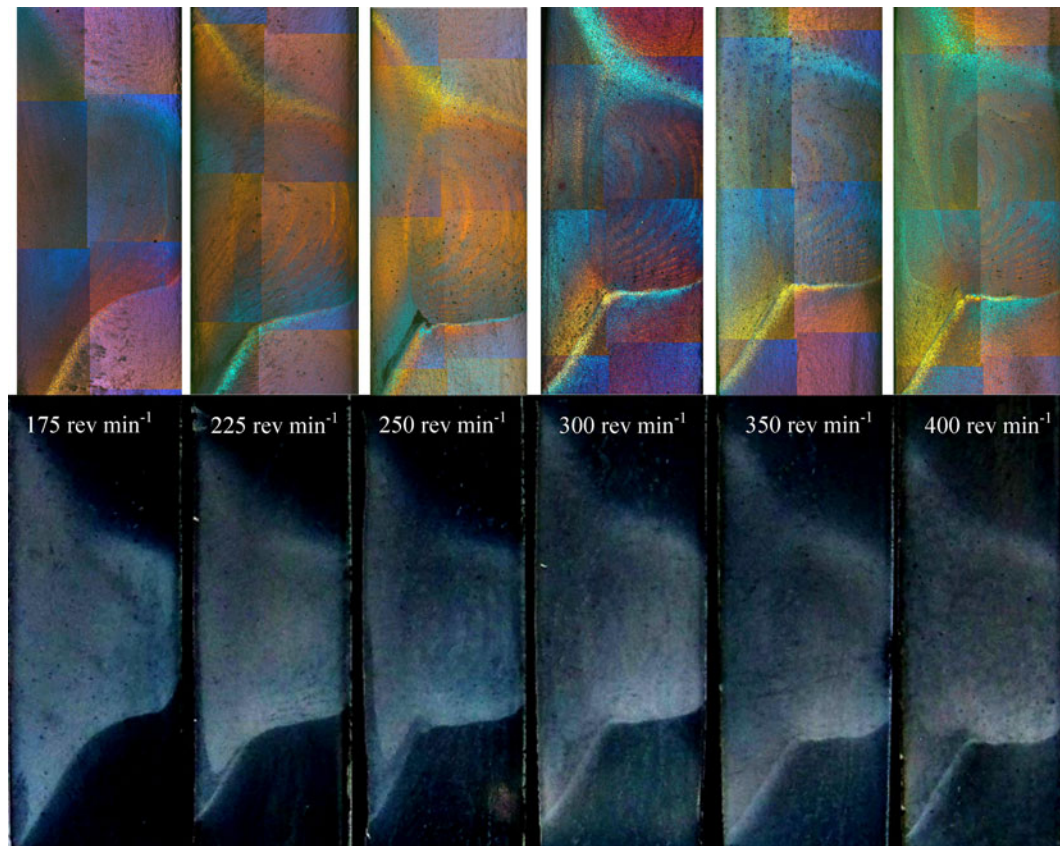


Fig. 10—Metallographic images of the weld zone for each weld condition (top images were anodized and observed under polarized light to enhance the onion appearance).

previously discussed, at  $250 \text{ rev min}^{-1}$ , the surface material slightly exceeds the peak exothermic transformation temperature, while the *in situ* material reaches a temperature in between the respective endothermic and exothermic temperatures. Before being introduced into the weld zone, the surface material will experience a strong precipitation of stable  $\eta$  and/or  $T$  phases, and the *in situ* material will dissolve fine GP and  $\eta'$ , which will re-precipitate upon cooling and holding at room temperature. The resulting microstructure will have defined bands of particle-rich surface material and particle-poor *in situ* material comprising the weld. Similarly at  $300 \text{ rev min}^{-1}$ , the surface material now exceeds the exothermic temperature by 52 K, and the *in situ* material temperature is effectively equal to the peak exothermic temperature. As such,  $\eta$  and/or  $T$  phases in the surface material will coarsen and begin to dissolve while they approach the maximum rate of precipitation in the *in situ* material. Suggesting that the volume fraction of these phases is the same for these two conditions, the surface material would have a smaller particle number density and a larger average particle size than the *in situ* material. Mixing the bands of surface material containing coarser  $\eta/T$  particles with the bands of *in situ* material containing finer  $\eta/T$  particles again imparts a strong onion ring pattern due to the optical contrast in precipitation.

For pin rotation speeds greater than  $300 \text{ rev min}^{-1}$ , both the *in situ* and surface material temperatures

exceed the respective peak exothermic phase transformation temperatures. For the surface material, the temperature of which now exceeds 673 K ( $400^\circ\text{C}$ ), the trend will be toward complete dissolution of the  $\eta$  and/or  $T$  phases and GP zone formation upon cooling and holding at room temperature. The *in situ* material will experience limited dissolution of the  $\eta$  and/or  $T$  phases as well, but since the temperature lags behind that of the surface material, some overaged  $\eta$  and/or  $T$  phases can be retained at room temperature. As a result, the onion ring pattern will become fainter for pin rotation speeds beyond  $300 \text{ rev min}^{-1}$ . The microstructural images for the 350 and  $400 \text{ rev min}^{-1}$  welds in Figure 10 show faint onion patterns, but they are certainly less distinct than those in the 250 and  $300 \text{ rev min}^{-1}$  welds.

The appearance of onion rings within the weld nugget is a well-established, but not fully understood, phenomenon in FSW. The terms “particle-rich” and “particle-poor” were originally introduced by Sutton *et al.*<sup>[29]</sup> who observed the onion ring phenomenon in FSW 2024 and determined the rings were interleaved bands of material both rich and depleted in secondary phases. Not all researchers, however, credit the formation of onion rings to disparate particle distributions. Rather, some researchers have concluded that the weld nugget structure is actually an interleaving of layers of fine-equiaxed, recrystallized grains with coarse recrystallized grains.<sup>[30, 31]</sup> Perhaps both hypotheses are actually correct and the mode of onion ring formation is simply dependent on

both the workpiece material and the welding conditions. For aluminum 7042-T6, at least, the formation of onion rings depends on the temperature of the surface material and *in situ* material relative to the endothermic and exothermic precipitate transformation temperatures, which are driven by the heating rates during friction stir welding. As the fine Al<sub>3</sub>(Sc,Zr) particles presented in the 7042-T6 alloy effectively suppress recrystallization, the onion rings are evidently not related to recrystallized grains in this material.

## V. CONCLUSIONS

A coupled thermal/material flow model of friction stir welding was developed and utilized to simulate the joining of Sc-modified aluminum extrusions (7042-T6). The model successfully predicts the temperatures in and near the weld zone for all weld conditions. For higher pin rotation speeds (300 rev min<sup>-1</sup> and greater), the model shows good agreement with the experimental temperature distribution within the workpiece away from the weld zone. For slower pin rotation speeds (250 rev min<sup>-1</sup> and less), however, the model overpredicts the workpiece temperatures away from the weld.

Within the weld zone, the model demonstrates that surface material approaching the rotating tool is swept to the retreating side. The material then (1) rotates with the tool under the shoulder and is deposited behind the tool toward the advancing side, (2) rotates under the shoulder and is captured by the tool, or (3) rotates under the shoulder and is pulled into the weld zone by the threaded pin. Mid-plane and bottom plane materials rotate with the tool and show some downward migration. The extrusion of “hotter” surface material into the weld nugget where it interleaves with “cooler” *in situ* material gives rise to the formation of onion rings in the 7042-T6 alloy. If the surface material temperature is greater than the exothermic transformation temperature of the alloy, then the surface becomes enriched in stable  $\eta$  and/or  $T$  phases before being pulled into the weld nugget. If, at the same time, the *in situ* material temperature is greater than the endothermic reaction temperature, but less than the exothermic reaction temperature, the *in situ* material becomes depleted in the non-equilibrium  $\eta'$  phase and supersaturated. Upon cooling, GP zones form in the *in situ* material, such that bands of particle-rich surface material interleaved with particle-poor *in situ* material comprise the weld nugget and impart the characteristic onion ring appearance.

## ACKNOWLEDGMENTS

The authors would like to acknowledge the Polish Ministry of Science and Higher Education (Grant No. N507 446337) and UES, Inc. for their support of this work. ONS acknowledges financial support through the United States Air Force Research Laboratory Contract No. FA8650-10-D-52226.

## OPEN ACCESS

This article is distributed under the terms of the Creative Commons Attribution License which permits any use, distribution, and reproduction in any medium, provided the original author(s) and the source are credited.

## REFERENCES

1. R. Nandan, T. DebRoy, and H.K.D.H. Bhadeshia: *Prog. Mater. Sci.*, 2008, vol. 53, pp. 980–1023.
2. P.L. Threadgill, A.J. Leonard, H.R. Shercliff, and P.J. Withers: *Int. Mater. Rev.*, 2009, vol. 54, pp. 49–93.
3. P.A. Colgrove and H.R. Shercliff: *Sci. Technol. Weld. Join.*, 2003, vol. 8, pp. 360–68.
4. M.Z.H. Khandkar, J.A. Khan, and A.P. Reynolds: *Sci. Technol. Weld. Join.*, 2003, vol. 8, pp. 165–74.
5. J.D. Robson and L. Campbell: *Sci. Technol. Weld. Join.*, 2010, vol. 15, pp. 171–76.
6. P.A. Colegrove, H.R. Shercliff, and R. Zettler: *Sci. Technol. Weld. Join.*, 2007, vol. 12, pp. 284–97.
7. S.V. Senkova, O.N. Senkov, and D.B. Miracle: *Metall. Mater. Trans. A*, 2006, vol. 57A, pp. 3569–75.
8. R.B. Bhat, J.D. Schloz, S.V. Senkova, and O.N. Senkov: *Metall. Mater. Trans. A*, 2005, vol. 36A, pp. 2115–26.
9. P.S. De and R.S. Mishra: *Sci. Technol. Weld. Join.*, 2011, vol. 16, pp. 343–47.
10. O.N. Senkov, M.R. Shagiev, and S.V. Senkova: *Metall. Mater. Trans. A*, 2008, vol. 39A, pp. 1034–53.
11. I.J. Polmear: *Light Alloys: From Traditional Alloys to Nanocrystals*, 4th ed, Elsevier Butterworth-Heinemann, London, 2006, pp. 131–60.
12. O.N. Senkov, M.R. Shagiev, S.V. Senkova, and D.B. Miracle: *Acta Mater.*, 2008, vol. 56, pp. 3723–38.
13. M.J. Starink: *Int. Mater. Rev.*, 2004, vol. 49, pp. 191–226.
14. V. Dixit, R.S. Mishra, R.J. Lederich, and R. Talwar: *Sci. Technol. Weld. Join.*, 2009, vol. 14, pp. 346–55.
15. V. Dixit, R.S. Mishra, R.J. Lederich, and R. Talwar: *Sci. Technol. Weld. Join.*, 2007, vol. 12, pp. 334–40.
16. O.C. Zienkiewicz and I.C. Cormeau: *Int. J. Numer. Methods. Eng.*, 1974, vol. 8, pp. 821–45.
17. O. Frigaard, O. Grong, and O.T. Midling: *Metall. Mater. Trans. A*, 2001, vol. 32A, pp. 1189–1200.
18. R. Nandan, G.G. Roy, and T. DebRoy: *Metall. Mater. Trans. A*, 2006, vol. 37A, pp. 1247–59.
19. A. Arora, Z. Zhang, A. De, and T. DebRoy: *Scripta Mater.*, 2009, vol. 61, pp. 863–66.
20. P. Heurtier, M.J. Jones, C. Desrayaud, J.H. Driver, F. Montheillet, and D. Allehaux: *J. Mater. Process. Tech.*, 2006, vol. 171, pp. 348–57.
21. T. Sheppard and D. Wright: *Met. Technol.*, 1979, vol. 6, pp. 215–23.
22. C. Hamilton, A. Sommers, and S. Dymek: *Int. J. Mach. Tool. Manu.*, 2009, vol. 49, pp. 230–38.
23. C. Hamilton, S. Dymek, and A. Sommers: *Int. J. Mach. Tool. Manu.*, 2008, vol. 48, pp. 1120–30.
24. C. Hamilton, S. Dymek, and M. Blicharski: *Mater. Charact.*, 2008, vol. 59, pp. 1206–14.
25. K. Colligan: *Weld. J.*, 1999, vol. 78, pp. 229S–37S.
26. A. Guerra, C. Schmidt, J.C. McClure, L.E. Murr, and A.C. Nunes: *Mat. Charact.*, 2002, vol. 49, pp. 95–101.
27. A.P. Reynolds: *Sci. Technol. Weld. Join.*, 2000, vol. 5, pp. 120–24.
28. C. Hamilton, S. Dymek, and O. Senkov: *Sci. Technol. Weld. Join.*, 2012, vol. 17, pp. 42–48.
29. M.A. Sutton, B. Yang, A.P. Reynolds, and R. Taylor: *Mater. Sci. Eng. A*, 2002, vol. 323, pp. 160–66.
30. W.M. Thomas, K.I. Johnson, and C.S. Wiesner: *Adv. Eng. Mater.*, 2003, vol. 5, pp. 485–90.
31. M.W. Mahoney, C.G. Rhodes, J.G. Flintoff, R.A. Spurling, and W.H. Bingel: *Metall. Mater. Trans. A*, 1998, vol. 29A, pp. 1955–64.